Editors' Suggestion

Raman Optical Activity Induced by Ferroaxial Order in $NiTiO_3$

Gakuto Kusuno,[1] Takeshi Hayashida,[2,3] Takayuki Nagai,[2] Hikaru Watanabe,[4,5] Rikuto Oiwa,[6,7]
Tsuyoshi Kimura,[2] and Takuya Satoh[1,8]
[1]*Department of Physics, Institute of Science Tokyo, Tokyo 152-8551, Japan*
[2]*Department of Applied Physics, The University of Tokyo, Tokyo 113-8656, Japan*
[3]*FELIX Laboratory, Radboud University, Toernooiveld 7, 6525 ED Nijmegen, The Netherlands*
[4]*Graduate School of Engineering, Hokkaido University, Sapporo 060-8628, Japan*
[5]*Department of Physics, The University of Tokyo, Tokyo 113-0033, Japan*
[6]*Graduate School of Science, Hokkaido University, Sapporo 060-0810, Japan*
[7]*Center for Emergent Matter Science, RIKEN, Wako, Saitama 351-0198, Japan*
[8]*Quantum Research Center for Chirality, Institute for Molecular Science, Aichi 444-8585, Japan*

(Received 28 May 2025; revised 23 December 2025; accepted 7 April 2026; published 19 May 2026)

Raman optical activity (ROA), the dependence of Raman intensity on the circular polarization of incident and scattered light, has traditionally been observed in chiral molecules and magnetic materials, where inversion or time-reversal symmetry is broken. Here we demonstrate that ROA can also arise in a centrosymmetric and nonmagnetic ferroaxial crystal. Using circularly polarized Raman spectroscopy on single-crystalline $NiTiO_3$, we observed a pronounced ROA signal in the cross-circular polarization configurations, which correlates with the ferroaxial domain structure. Our symmetry analysis, first-principles calculations of phonons, and tight-binding model calculations reveal that the natural ROA originates from the ferroaxial order and persists even within the electric dipole approximation. These results establish ROA as a powerful probe of ferroaxial order in centrosymmetric systems.

DOI: 10.1103/wrv8-4f7k

Chirality is the property of objects that cannot be superimposed on their mirror images by rotation, as exemplified by left and right hands. It is widespread in nature and occurs in crystals with helical structures. When light enters such chiral materials, it gives rise to optical rotation and circular dichroism, phenomena collectively known as natural electronic optical activity (NEOA) [1]. The sense of rotation of linearly polarized light and the differential absorption of left- and right-circularly polarized light vary with the handedness of the chiral material. Therefore, NEOA serves as a valuable technique for probing chirality.

A similar phenomenon occurs in Raman scattering, known as Raman optical activity (ROA), which involves differences in the Raman intensities depending on the circular polarization state of the incident and scattered light. ROA has been reported in systems containing chiral molecules and in those with magnetic ordering. ROA arising from magnetic effects is referred to as magnetic ROA, while that occurring in nonmagnetic materials is called natural ROA (NROA) [1]. The NROA of chiral molecules is attributed to the interference between scattered light resulting from electric dipole-electric dipole transitions and that from electric dipole-magnetic dipole transitions [2]. For NROA to occur, the materials have traditionally been thought to lack inversion symmetry.

However, recent experimental studies suggest that NROA can also be observed in centrosymmetric, nonmagnetic materials. In the layered compound $1T$-TaS_2, intensity differences between left- and right-circularly polarized Raman spectra have been observed in the chiral charge density wave (CDW) phase [3–6]. Despite its name, the chiral CDW phase of $1T$-TaS_2 is not strictly chiral, as its point group, $\bar{3}$, is achiral and retains inversion symmetry. This state is more accurately described as exhibiting ferroaxial (ferrorotational) order [6]. Previous studies have attributed the origin of ROA in this material to chiral CDW domains formed through complex Raman tensors owing to optical absorption [4]. Similar circular intensity differences in Raman scattering have also been reported in compounds that are both chiral and polar, such as $NiCo_2TeO_6$, which belongs to the ferroaxial point group 3 [7]. However, the microscopic mechanism by which NROA arises from ferroaxial order remains unknown.

In this Letter, we report the observation of a remarkably large ROA in a three-dimensional centrosymmetric bulk crystal of $NiTiO_3$, a material known to exhibit ferroaxial order. The intensity differences observed in both the Stokes and anti-Stokes spectra are consistent with the symmetry arguments of NROA. Furthermore, our calculations show that the observed NROA originates directly from the ferroaxial order.

Ferroaxial order was proposed as a type of ferroic order that is invariant under both spatial inversion and time-reversal operations [8]. It arises from the breaking mirror

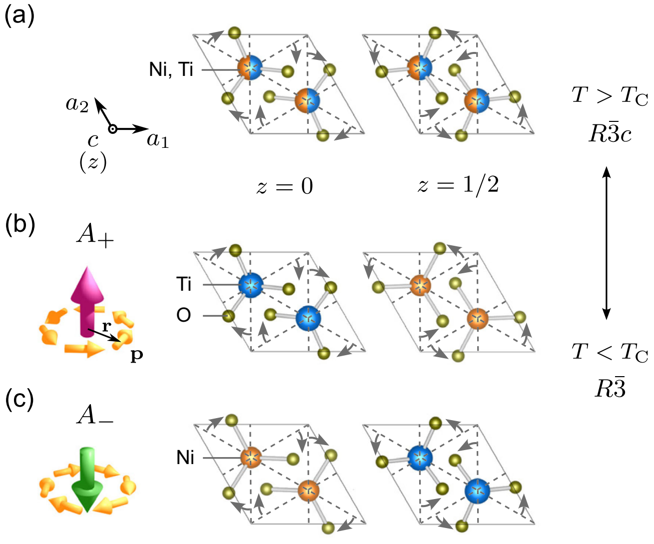

FIG. 1. (a) Crystal structure of $NiTiO_3$ above the structural phase transition temperature ($T_C = 1560$ K). Ti and Ni cations on $z = 0$ and $z = 1/2$ layers and oxygen ions bonded to them are depicted. (b),(c) Crystal structures viewed along the c axis for the A_+ and A_- ferroaxial domains, respectively. The gray arrows denote the direction of rotational displacements of oxygen ions from the (110)-type planes (dotted lines). The ferroaxial order, indicated by the purple or green arrows, is characterized as $\mathbf{A} \propto \sum_i \mathbf{r}_i \times \mathbf{p}_i$, where $\mathbf{r}_i$ and $\mathbf{p}_i$ are the position vector and the electric dipole moment (yellow arrows) at site i, respectively (see the Supplemental Material, Sec. S1 [22] for details).

symmetry, with the mirror plane(s) obtained parallel to the principal axis. The order parameter is the axial vector $\mathbf{A} \propto \sum_i \mathbf{r}_i \times \mathbf{p}_i$, where $\mathbf{r}_i$ and $\mathbf{p}_i$ represent the position vector and electric dipole moment of the ith atom, respectively [9]. Such axial vectors are allowed in only 13 of the 32 crystal point groups [10,11]. Since chirality-related phenomena, such as NEOA, require the breaking of inversion symmetry, some ferroaxial materials with centrosymmetric structures do not exhibit NEOA. Well-known ferroaxial systems that retain inversion symmetry include $RbFe(MoO_4)_2$ [12], $K_2Zr(PO_4)_2$ [13,14], $NiTiO_3$ [15–18], and $MnTiO_3$ [19,20].

In $NiTiO_3$, the high-temperature phase above the transition temperature $T_C = 1560$ K adopts a corundum-type structure, where Ni^{2+} and Ti^{4+} ions are randomly distributed at the cation sites [Fig. 1(a)]. The space group is $R\bar{3}c$ (point group $\bar{3}m$), and the structure lacks ferroaxial order due to the presence of a glide (mirror) plane along the principal axis. As the temperature decreases, a structural phase transition occurs at T_C [15,21]. Below T_C, the Ni^{2+} and Ti^{4+} ions become ordered. The space group changes to $R\bar{3}$ (point group $\bar{3}$), breaking the mirror symmetry. Consequently, a net axial vector emerges. The A_+ and A_- domain states shown in Figs. 1(b) and 1(c), respectively, correspond to different axial vector orientations and are related by a c-glide operation or by flipping the crystal along the c axis.

We prepared both single- and multidomain crystals of $NiTiO_3$. A single-domain crystal grown using the flux method [45] was 60 μm thick and was confirmed to be a single domain by electrogyration measurements [15,46]. A multidomain crystal was obtained by heating a single-domain crystal to 1620 K and then slowly cooling it, resulting in a mixture of ferroaxial domains. This domain structure was also confirmed via electrogyration, as reported in Ref. [46].

We performed circularly polarized Raman spectroscopy in a backscattering geometry with excitation along the c axis using 785, 532, and 633 nm lasers. The detailed setup is shown in the Supplemental Material [22], Sec. S2. In the wavelength range around 785 nm, a strong absorption occurs due to d-d transitions of the Ni^{2+} ions, whereas the absorption at 532 nm is much weaker and originates from the tail of a charge-transfer transition band. At 633 nm, the absorption is minimal [47]. The scattered light was collected through an objective lens, filtered to remove Rayleigh scattering using edge or notch filters, and detected with a CCD-equipped spectrometer. All measurements were performed at 295 K, which is far above the antiferromagnetic Néel temperature, $T_N = 22.5$ K [48]. Left (L) and right (R) circular polarizations were defined based on the rotation of the electric field on the sample plane, independent of the propagation direction. Four polarization configurations for the incident and scattered light were considered: LR and RL (cross circular) and LL and RR (parallel circular), as shown in Figs. 2(a) and 2(b), respectively. According to the polarization selection rules for Raman-active modes $\Gamma = 5A_g \oplus 5E_g$, E_g-mode phonons are active in cross-circular polarization configurations, whereas A_g modes are active in parallel-circular polarization configurations (see the Supplemental Material [22], Sec. S3 for details).

Raman spectra obtained from the front surface of the single-domain crystal at an excitation wavelength of 785 nm for the RL and LL configurations are shown in Fig. 2(c). Four A_g and five E_g modes were identified. The assignment of these modes agrees well with those reported in previous studies on $NiTiO_3$ powders [23,49]. Although the $A_g^{(4)}$ mode has been reported to exist near 480 cm^{-1} and was confirmed by our first-principles calculations (see the Supplemental Material [22], Sec. S4 for details), it was not experimentally observed due to its weak intensity.

Next, we conducted measurements in the cross-circular polarization (LR and RL) configurations. The Raman spectra from the front surface of the single-domain crystal at an excitation wavelength of 785 nm are shown in Figs. 3(a) and 3(b), respectively. All five phonon peaks corresponding to E_g modes are observed in both the Stokes and anti-Stokes spectra. These peaks exhibit clear intensity differences between the LR and RL configurations. This result demonstrates that ROA occurs even in a centrosymmetric, achiral crystal, $NiTiO_3$. To quantify the ROA, we defined the

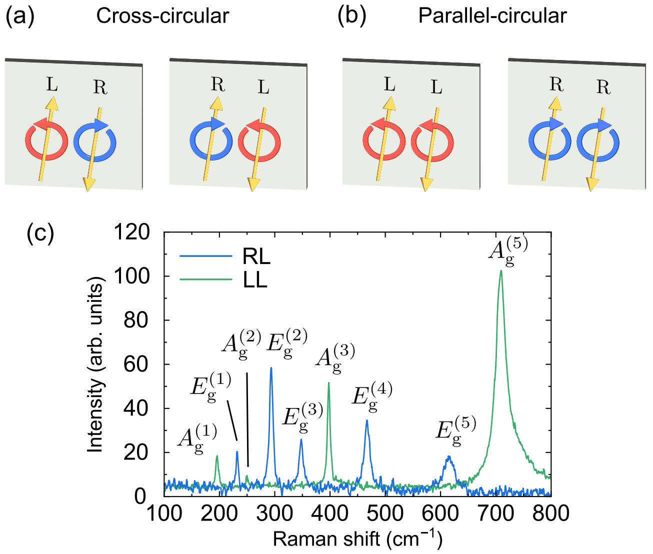

FIG. 2. (a),(b) Experimental setups for circularly polarized Raman spectroscopy in the cross-circular and parallel-circular polarization configurations, respectively. (c) Raman spectra of the single-domain $NiTiO_3$ crystal, measured at 295 K using 785 nm excitation in RL (R-incident, L-scattered) and LL (L-incident, L-scattered) configurations, with phonon mode assignments.

normalized intensity difference between the cross-circular polarization configurations as

$$g_{\mathrm{ROA}} = \frac{I_{\mathrm{LR}} - I_{\mathrm{RL}}}{(I_{\mathrm{LR}} + I_{\mathrm{RL}})/2}, \tag{1}$$

where I_{LR} and I_{RL} are the Raman intensities of the LR and RL configurations, respectively. The value of g_{ROA} varies across the phonon modes, with the $E_g^{(1)}$ mode exhibiting the largest intensity difference, reaching $g_{\mathrm{ROA}} \simeq 1.0$. This value is several orders of magnitude larger than the typical NROA of chiral molecules, where $g_{\mathrm{ROA}} \sim 10^{-3}$ [2] (see the Supplemental Material [22], Table S4 in Sec. S5, for the values of g_{ROA} for the other peaks). The identical sign of g_{ROA} in the Stokes and anti-Stokes spectra indicates that the observed ROA in $NiTiO_3$ is nonmagnetic in origin, in contrast to magnetic ROA where the sign reverses [50–52].

Figures 3(c) and 3(d) show Raman spectra measured on the back surface of the same single-domain crystal. We again observed intensity differences between the LR and RL configurations; however, the sign of g_{ROA} was reversed compared to the front side. This indicates that the observed NROA in $NiTiO_3$ is direction dependent—i.e., it depends on the orientation (sign) of the ferroaxial vector. Such directionality does not originate from the bulk properties of chiral materials. Instead, it reflects the domain-dependent orientation of the ferroaxial order, which differs between the front and back of the crystal. The differential Raman spectra of cross-circular polarization configurations on the front and back surfaces are shown in Fig. S6 of the Supplemental Material [22], Sec. S6.

In contrast to the E_g modes, no noticeable intensity differences were observed for the A_g modes in the parallel-circular polarization (LL and RR) configurations (Fig. S7 in the Supplemental Material [22], Sec. S7). Moreover, the E_g modes excited at a wavelength of 532 nm exhibited only weak intensity differences and no discernable intensity differences at 633 nm (see the Supplemental Material [22], Sec. S5). These results suggest that NROA is selectively enhanced in certain phonon modes due to coupling with the electronic structure associated with the ferroaxial order.

The selective enhancement of ROA at 785 nm can be understood as a cooperative effect of (i) symmetry and (ii) resonance. From (i) the symmetry perspective, the E_g phonons are decomposed into two components, ${}^1E_g$ and ${}^2E_g$, corresponding to counterclockwise and clockwise rotational motions with crystal angular or pseudo-angular

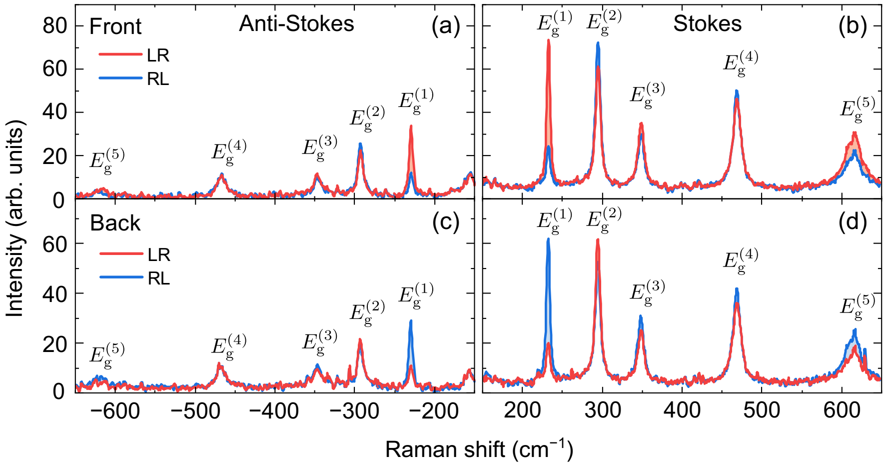

FIG. 3. Raman spectra of the front (a),(b) and back (c),(d) surfaces of the single-domain $NiTiO_3$ crystal, measured at 295 K using 785 nm excitation in LR and RL configurations. (a),(c) show anti-Stokes spectra, while (b),(d) show Stokes spectra.

momenta of $+1$ and -1, respectively. Under circularly polarized excitation, the LR and RL configurations transfer angular momenta of -2 and $+2$ to the material, thereby selectively exciting the ${}^1E_g$ and ${}^2E_g$ phonons in accordance with angular momentum conservation and the Umklapp process in the threefold symmetry [24].

The Raman intensity in the electric dipole approximation can be expressed as $I \propto |\mathbf{e}_s^{\dagger} R \mathbf{e}_i|^2$, where $\mathbf{e}_i$ and $\mathbf{e}_s$ are the polarization vectors of the incident and scattered light, respectively, and R is the Raman tensor. The Raman tensor for the E_g phonons are given by

$$R = R_1 \begin{pmatrix} 1 & i \\ i & -1 \end{pmatrix} + R_2 \begin{pmatrix} 1 & -i \\ -i & -1 \end{pmatrix}, \tag{2}$$

where R_1 and R_2 are proportional coefficients of the Raman tensor for phonon modes belonging to ${}^1E_g$ and ${}^2E_g$, respectively (see the Supplemental Material [22], Sec. S3 for derivations). Since the Raman intensities in the LR and RL configurations are proportional to $|R_1|^2$ and $|R_2|^2$, respectively, a nonzero ROA arises when $|R_1| \neq |R_2|$. The static ferroaxial distortion provides a preferred sense of rotation in the lattice, rendering the two rotational components, ${}^1E_g$ and ${}^2E_g$, inequivalent and leading to asymmetric Raman tensor elements ($|R_1| \neq |R_2|$), which in turn give rise to a finite ROA signal.

For (ii) resonance, at 785 nm the incident light is resonant with the Ni^{2+} d-d transition. This transition is electric-dipole allowed because the local inversion symmetry at the Ni site is already broken. The ferroaxial rotational distortion further lowers the local symmetry from $3m$ to 3, which modifies the symmetry of the lattice displacements coupled to the d-d transition. Under this resonance, the intermediate electronic states involved in Raman scattering are highly sensitive to local lattice distortions. Our first-principles calculations show that the $E_g^{(1)}$ mode involves the largest displacement of Ni^{2+} ions, leading to the strongest coupling to the resonant transition and accounting for the largest observed ROA at 785 nm.

We verified the condition $|R_1| \neq |R_2|$ in ferroaxial systems using symmetry-based model calculations. Specifically, we consider a tight-binding Hamiltonian for spinless p orbitals on a trigonal lattice with symmetry-adapted bases [25] and demonstrate that ferroaxial rotation generically leads to different scattering amplitudes in the two cross-circular polarization configurations, independent of microscopic band details. Regarding the Raman tensors $R(\omega, \delta\omega)$ with their explicit dependence on the frequency of the incident light ω and the (anti-)Stokes shift $\delta\omega$, we numerically computed the ω dependence of the coefficients $R_i (i = 1, 2)$. Following the established perturbation calculations within the electric dipole approximation, we obtained the normalized cross-circular Raman intensities, defined as

$$\bar{I}_{\mathrm{LR}} = \frac{|R_1|^2}{|R_1|^2 + |R_2|^2}, \qquad \bar{I}_{\mathrm{RL}} = \frac{|R_2|^2}{|R_1|^2 + |R_2|^2}. \tag{3}$$

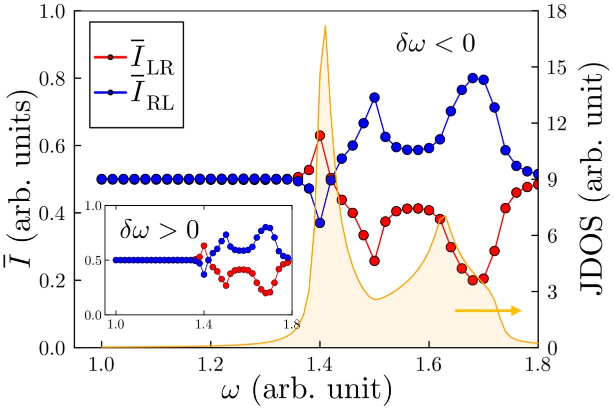

FIG. 4. Excitation frequency (ω) dependence of the normalized cross-circular Raman scattering intensities ($\bar{I}_{\mathrm{LR}}, \bar{I}_{\mathrm{RL}}$) and the joint density of states (JDOS) obtained from model calculations. JDOS indicates the number of optically resonant states contributing to the Raman scattering. Main plots of $\bar{I}_{\mathrm{LR}}, \bar{I}_{\mathrm{RL}}$ are for the Stokes process ($\delta\omega = -10^{-3} < 0$), and the inset is for the anti-Stokes process ($\delta\omega = 10^{-3} > 0$).

In Fig. 4, we observe a significant deviation between the two intensities ($\bar{I}_{\mathrm{LR}} \neq \bar{I}_{\mathrm{RL}}$), indicating a cross-circular ROA even within the electric dipole approximation. Analysis of the essential parameters [26] shows that the cross-circular ROA results from the coupling of the E_g phonons to the orbital rotations driven by the ferroaxial order (see the Supplemental Material [22], Sec. S8 for details). ROA is strongly enhanced in the presence of resonant particle-hole excitations, as illustrated by the JDOS, supporting the experimental results obtained with different light sources (Fig. 3 and the Supplemental Material [22], Sec. S5). Notably, consistent with experimental observations, the signs of the cross-circular ROA ($\bar{I}_{\mathrm{LR}} - \bar{I}_{\mathrm{RL}}$) are the same for the Stokes ($\delta\omega < 0$) and anti-Stokes ($\delta\omega > 0$) responses for each excitation frequency ω (Fig. 4 and inset). Note that although the model calculation was conducted on a trigonal lattice, our symmetry analysis can extend to ferroaxial systems with n-fold rotational symmetry ($n = 1, 2, 3, 4, 6$), provided that the Raman susceptibility differs between the two cross-circular polarization configurations.

To further confirm that the observed intensity differences reflect the ferroaxial order in $\mathrm{NiTiO_3}$, we performed a spatial mapping of g_{ROA} by scanning the laser spot across the sample. Figures 5(a) and 5(b) show spatial maps of g_{ROA} near the $E_g^{(1)}$ peak on the front and back surfaces of a single-domain crystal, respectively. The sign of g_{ROA} is reversed between the two surfaces, which is consistent with the change in the ferroaxial domain orientation. In the regions outside the sample or near cracks, $g_{\mathrm{ROA}} \sim 0$, indicating that the observed ROA was intrinsic and not

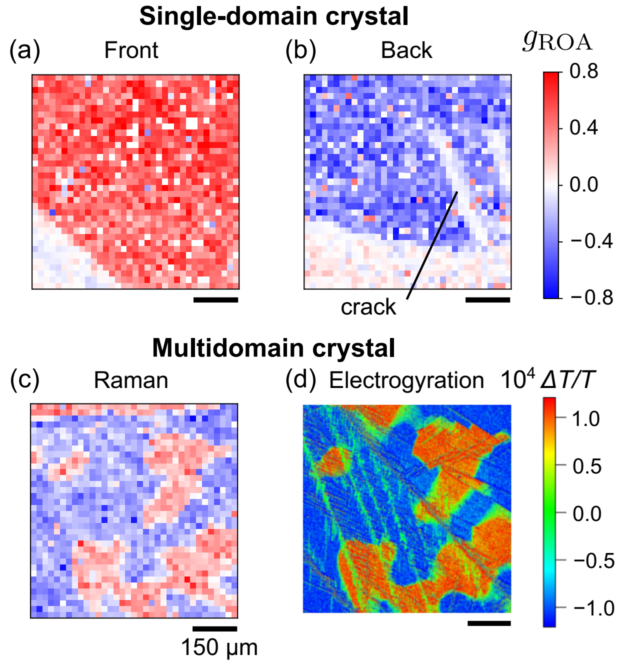

FIG. 5. Imaging of ferroaxial domains in $\mathrm{NiTiO_3}$. (a),(b) Domain maps of the front and back surfaces of a single-domain crystal obtained by circularly polarized Raman spectroscopy. (c) Domain map of a multidomain crystal. The normalized intensity difference $g_{\mathrm{ROA}} = 2(I_{\mathrm{LR}} - I_{\mathrm{RL}})/(I_{\mathrm{LR}} + I_{\mathrm{RL}})$ of the $E_g^{(1)}$ peak is plotted. (d) Domain image obtained by electrogyration, adapted from Ref. [46] (image inverted from the original).

due to instrumental offsets. Figure 5(c) shows a similar mapping for a multidomain crystal, revealing a domain pattern with features on the order of 100 μm. This pattern closely matches the ferroaxial domain distribution obtained from electrogyration imaging [Fig. 5(d)] as reported in Ref. [46], which supports the conclusion that the ROA reflects the ferroaxial order. The narrow region where g_{ROA} approaches zero likely reflects either partial averaging of A_+ and A_- domains within the optical spot or a suppression of the ferroaxial order at the domain wall; higher spatial resolution would be required to distinguish these scenarios (see the Supplemental Material [22], Sec. S9).

In summary, we demonstrated a remarkably large ROA in the ferroaxial crystal $\mathrm{NiTiO_3}$ using circularly polarized Raman spectroscopy. The intensity differences observed in the Stokes and anti-Stokes spectra, together with their dependence on the domain orientation, provide clear evidence that the ROA is induced by ferroaxial order. Our calculations show that this effect arises from intrinsic electron-phonon coupling within the electric dipole approximation, even in centrosymmetric, achiral, and non-magnetic materials. These findings pave the way for the observation of ferroaxial domains using Raman spectroscopy and broaden the scope of ROA beyond chiral and magnetic systems. Furthermore, the coupling between electrons and chiral phonons in $\mathrm{NiTiO_3}$ is expected to give rise to diverse phenomena, including phonon magnetic moments [53,54].

Acknowledgments—We thank K. T. Yamada for technical assistance, and H. Kusunose, H. Yokota, and R. Arita for valuable discussions. T. S. was supported in part by JSPS KAKENHI (Grants No. JP21H01032, No. JP22H01154, and No. JP26H02234), MEXT X-NICS (Grant No. JPJ011438), NINS OML Project (Grant No. OML012301), JST CREST (Grant No. JPMJCR24R5), and JST ERATO (Grant No. JPMJER2503). T. K. was supported in part by JSPS KAKENHI (Grants No. JP25H00392 and No. JP25H01247). H. W. was supported by JSPS KAKENHI (Grants No. JP23K13058, No. JP24K00581, and No. JP25H02115) and by RIKEN TRIP initiative (RIKEN Quantum, Advanced General Intelligence for Science Program, Many-Body Electron Systems). R. O. was supported by a Special Postdoctoral Researcher Program at RIKEN. G. K. was supported by JST SPRING (Grant No. JPMJSP2180) and the Science Tokyo Support Program for Doctoral Students, funded by the Universities for International Research Excellence. We used VESTA [55] to visualize the crystal structures.

Data availability—The data that support the findings of this article are available in the Supplemental Material.

---

[1] L. D. Barron, *Molecular Light Scattering and Optical Activity*, 2nd ed. (Cambridge University Press, Cambridge, England, 2004).

[2] L. D. Barron and A. D. Buckingham, Rayleigh and Raman scattering from optically active molecules, Mol. Phys. **20**, 1111 (1971).

[3] E. M. Lacinska, M. Furman, J. Binder, I. Lutsyk, P. J. Kowalczyk, R. Stepniewski, and A. Wysmolek, Raman optical activity of 1T-$\mathrm{TaS_2}$, Nano Lett. **22**, 2835 (2022).

[4] H. F. Yang, K. Y. He, J. Koo, S. W. Shen, S. H. Zhang, G. Liu, Y. Z. Liu, C. Chen, A. J. Liang, K. Huang, M. X. Wang, J. J. Gao, X. Luo, L. X. Yang, J. P. Liu, Y. P. Sun, S. C. Yan, B. H. Yan, Y. L. Chen, X. Xi, and Z. K. Liu, Visualization of chiral electronic structure and anomalous optical response in a material with chiral charge density waves, Phys. Rev. Lett. **129**, 156401 (2022).

[5] Y. Zhao, Z. Nie, H. Hong, X. Qiu, S. Han, Y. Yu, M. Liu, X. Qiu, K. Liu, S. Meng, L. Tong, and J. Zhang, Spectroscopic visualization and phase manipulation of chiral charge density waves in 1T-$\mathrm{TaS_2}$, Nat. Commun. **14**, 2223 (2023).

[6] G. Liu, T. Qiu, K. He, Y. Liu, D. Lin, Z. Ma, Z. Huang, W. Tang, J. Xu, K. Watanabe, T. Taniguchi, L. Gao, J. Wen, J.-M. Liu, B. Yan, and X. Xi, Electrical switching of ferro-rotational order in nanometre-thick 1T-$\mathrm{TaS_2}$ crystals, Nat. Nanotechnol. **18**, 854 (2023).

[7] V. A. Martinez, Y. Gao, J. Yang, F. Lyzwa, Z. Liu, C. J. Won, K. Du, V. Kiryukhin, S. W. Cheong, and A. A. Sirenko, Ferroaxial phonons in chiral and polar $\mathrm{NiCo_2TeO_6}$, Phys. Rev. B **112**, 064411 (2025).

[8] R. D. Johnson, S. Nair, L. C. Chapon, A. Bombardi, C. Vecchini, D. Prabhakaran, A. T. Boothroyd, and P. G. Radaelli, $Cu_3Nb_2O_8$: A multiferroic with chiral coupling to the crystal structure, Phys. Rev. Lett. **107**, 137205 (2011).

[9] S.-W. Cheong, D. Talbayev, V. Kiryukhin, and A. Saxena, Broken symmetries, non-reciprocity, and multiferroicity, npj Quantum Mater. **3**, 19 (2018).

[10] J. Hlinka, J. Privratska, P. Ondrejkovic, and V. Janovec, Symmetry guide to ferroaxial transitions, Phys. Rev. Lett. **116**, 177602 (2016).

[11] S. Hayami, M. Yatsushiro, Y. Yanagi, and H. Kusunose, Classification of atomic-scale multipoles under crystallographic point groups and application to linear response tensors, Phys. Rev. B **98**, 165110 (2018).

[12] W. Jin, E. Drueke, S. Li, A. Admasu, R. Owen, M. Day, K. Sun, S.-W. Cheong, and L. Zhao, Observation of a ferro-rotational order coupled with second-order nonlinear optical fields, Nat. Phys. **16**, 42 (2020).

[13] S. Yamagishi, T. Hayashida, R. Misawa, K. Kimura, M. Hagihala, T. Murata, S. Hirose, and T. Kimura, Ferroaxial transitions in glaserite-type compounds: Database screening, phonon calculations, and experimental verification, Chem. Mater. **35**, 747 (2023).

[14] S. Bhowal and N. A. Spaldin, Electric toroidal dipole order and hidden spin polarization in ferroaxial materials, Phys. Rev. Res. **6**, 043141 (2024).

[15] T. Hayashida, Y. Uemura, K. Kimura, S. Matsuoka, D. Morikawa, S. Hirose, K. Tsuda, T. Hasegawa, and T. Kimura, Visualization of ferroaxial domains in an order-disorder type ferroaxial crystal, Nat. Commun. **11**, 4582 (2020).

[16] H. Yokota, T. Hayashida, D. Kitahara, and T. Kimura, Three-dimensional imaging of ferroaxial domains using circularly polarized second harmonic generation microscopy, npj Quantum Mater. **7**, 106 (2022).

[17] X. Guo, R. Owen, A. Kaczmarek, X. Fang, C. De, Y. Ahn, W. Hu, N. Agarwal, S. H. Sung, R. Hovden, S.-W. Cheong, and L. Zhao, Ferrorotational domain walls revealed by electric quadrupole second harmonic generation microscopy, Phys. Rev. B **107**, L180102 (2023).

[18] T. Hayashida, K. Kimura, and T. Kimura, Electric field–induced magnetochiral dichroism in a ferroaxial crystal, Proc. Natl. Acad. Sci. U.S.A. **120**, e2303251120 (2023).

[19] D. Sekine, T. Sato, Y. Tokunaga, T. Arima, and M. Matsubara, Second harmonic imaging of antiferromagnetic domains and confirmation of absence of ferroaxial twins in $MnTiO_3$, Phys. Rev. Mater. **8**, 064406 (2024).

[20] X. Zhang, T. Carbin, K. Du, B. Li, K. Wang, C. Li, T. Qian, N. Ni, S.-W. Cheong, and A. Kogar, Directionally asymmetric nonlinear optics in ferrorotational $MnTiO_3$, Phys. Rev. B **112**, L121108 (2025).

[21] M. Lerch, H. Boysen, R. Neder, F. Frey, and W. Laqua, Neutron scattering investigation of the high temperature phase transition in $NiTiO_3$, J. Phys. Chem. Solids **53**, 1153 (1992).

[22] See Supplemental Material http://link.aps.org/supplemental/10.1103/wrv8-4f7k for experimental results of parallel-circular polarization configurations and exciting wavelength of 532 and 633 nm, first-principles calculations of phonons, derivations of Raman tensors and details of model calculations, which includes Refs. [23–44].

[23] Y. Tatsumi, T. Kaneko, and R. Saito, Conservation law of angular momentum in helicity-dependent Raman and Rayleigh scattering, Phys. Rev. B **97**, 195444 (2018).

[24] K. Ishito, H. Mao, Y. Kousaka, Y. Togawa, S. Iwasaki, T. Zhang, S. Murakami, J. Kishine, and T. Satoh, Truly chiral phonons in α-HgS, Nat. Phys. **19**, 35 (2023).

[25] M. S. Dresselhaus, G. Dresselhaus, and A. Jorio, *Group theory: Application to the Physics of Condensed Matter* (Springer Science & Business Media, New York, 2007).

[26] A. Jorio, R. Saito, G. Dresselhaus, and M. S. Dresselhaus, *Raman Spectroscopy in Graphene Related Systems*, 1st ed. (Wiley, New York, 2011).

[27] P. E. Blöchl, Projector augmented-wave method, Phys. Rev. B **50**, 17953 (1994).

[28] G. Kresse and J. Furthmüller, Efficient iterative schemes for ab initio total-energy calculations using a plane-wave basis set, Phys. Rev. B **54**, 11169 (1996).

[29] G. Kresse and D. Joubert, From ultrasoft pseudopotentials to the projector augmented-wave method, Phys. Rev. B **59**, 1758 (1999).

[30] J. P. Perdew, K. Burke, and M. Ernzerhof, Generalized gradient approximation made simple, Phys. Rev. Lett. **77**, 3865 (1996).

[31] S. L. Dudarev, G. A. Botton, S. Y. Savrasov, C. J. Humphreys, and A. P. Sutton, Electron-energy-loss spectra and the structural stability of nickel oxide: An LSDA + U study, Phys. Rev. B **57**, 1505 (1998).

[32] F. Zhou, M. Cococcioni, C. A. Marianetti, D. Morgan, and G. Ceder, First-principles prediction of redox potentials in transition-metal compounds with LDA + U, Phys. Rev. B **70**, 235121 (2004).

[33] A. Togo and I. Tanaka, First principles phonon calculations in materials science, Scr. Mater. **108**, 1 (2015).

[34] M. A. Ruiz Preciado, A. Kassiba, A. Morales-Acevedo, and M. Makowska-Janusik, Vibrational and electronic peculiarities of $NiTiO_3$ nanostructures inferred from first principle calculations, RSC Adv. **5**, 17396 (2015).

[35] R. Tursun, Y. Su, Q. Yu, J. Tan, T. Hu, Z. Luo, and J. Zhang, Effect of doping on the structural, magnetic, and ferroelectric properties of $Ni_{1-x}A_xTiO_3$ ($A = Mn$, Fe, Co, Cu, Zn; $x = 0, 0.05$, and 0.1), J. Alloys Compd. **773**, 288 (2019).

[36] W. Qi, A. Mattursun, M. Gao, A. Hushur, and H. Zhang, Lattice dynamics of $NiTiO_3$ under high pressure: Raman evidence under two pressure-transmitting mediums, Results Phys. **43**, 106114 (2022).

[37] L. Zhang and Q. Niu, Angular momentum of phonons and the Einstein–de Haas effect, Phys. Rev. Lett. **112**, 085503 (2014).

[38] K. Ishito, H. Mao, K. Kobayashi, Y. Kousaka, Y. Togawa, H. Kusunose, J. Kishine, and T. Satoh, Chiral phonons: Circularly polarized Raman spectroscopy and ab initio calculations in a chiral crystal tellurium, Chirality **35**, 338 (2023).

[39] E. Oishi, Y. Fujii, and A. Koreeda, Selective observation of enantiomeric chiral phonons in α-quartz, Phys. Rev. B **109**, 104306 (2024).

[40] H. Kusunose, R. Oiwa, and S. Hayami, Symmetry-adapted modeling for molecules and crystals, Phys. Rev. B **107**, 195118 (2023).

[41] J. A. Koningstein and O. S. Mortensen, Experimental observation of an antisymmetric Raman scattering tensor, Nature (London) **217**, 445 (1968).

[42] O. S. Mortensen and J. A. Koningstein, Electronic Raman effect. II. Asymmetry of the scattering tensor for electronic Raman transitions, J. Chem. Phys. **48**, 3971 (1968).

[43] S. Hayami, R. Oiwa, and H. Kusunose, Electric ferro-axial moment as nanometric rotator and source of longitudinal spin current, J. Phys. Soc. Jpn. **91**, 113702 (2022).

[44] R. Oiwa and H. Kusunose, Systematic analysis method for nonlinear response tensors, J. Phys. Soc. Jpn. **91**, 014701 (2022).

[45] G. Garton, S. Smith, and B. M. Wanklyn, Crystal growth from the flux systems PbO-V_2O_5 and Bi_2O_3-V_2O_5, J. Cryst. Growth **13–14**, 588 (1972).

[46] T. Hayashida, Y. Uemura, K. Kimura, S. Matsuoka, M. Hagihala, S. Hirose, H. Morioka, T. Hasegawa, and T. Kimura, Phase transition and domain formation in ferroaxial crystals, Phys. Rev. Mater. **5**, 124409 (2021).

[47] M.-W. Li, J.-P. Yuan, X.-M. Gao, E.-Q. Liang, and C.-Y. Wang, Structure and optical absorption properties of $NiTiO_3$ nanocrystallites, Appl. Phys. A **122**, 725 (2016).

[48] K. Dey, S. Sauerland, J. Werner, Y. Skourski, M. Abdel-Hafiez, R. Bag, S. Singh, and R. Klingeler, Magnetic phase diagram and magnetoelastic coupling of $NiTiO_3$, Phys. Rev. B **101**, 195122 (2020).

[49] Y. Fujioka, J. Frantti, A. Puretzky, and G. King, Raman study of the structural distortion in the $Ni_{1-x}Co_xTiO_3$ solid solution, Inorg. Chem. **55**, 9436 (2016).

[50] L. D. Barron, Anti-stokes Raman optical activity, Mol. Phys. **31**, 1929 (1976).

[51] L. D. Barron and J. Vrbancich, Anti-stokes magnetic Raman optical activity and time reversal, Chem. Phys. Lett. **92**, 466 (1982).

[52] J. Cenker, B. Huang, N. Suri, P. Thijssen, A. Miller, T. Song, T. Taniguchi, K. Watanabe, M. A. McGuire, D. Xiao, and X. Xu, Direct observation of two-dimensional magnons in atomically thin CrI_3, Nat. Phys. **17**, 20 (2021).

[53] D. M. Juraschek, M. Fechner, A. V. Balatsky, and N. A. Spaldin, Dynamical multiferroicity, Phys. Rev. Mater. **1**, 014401 (2017).

[54] D. Lujan, J. Choe, S. Chaudhary, G. Ye, C. Nnokwe, M. Rodriguez-Vega, J. He, F. Y. Gao, T. N. Nunley, E. Baldini, J. Zhou, G. A. Fiete, R. He, and X. Li, Spin–orbit exciton–induced phonon chirality in a quantum magnet, Proc. Natl. Acad. Sci. U.S.A. **121**, e2304360121 (2024).

[55] K. Momma and F. Izumi, VESTA3 for three-dimensional visualization of crystal, volumetric and morphology data, J. Appl. Crystallogr. **44**, 1272 (2011).